RESEARCH ARTICLE

Grain Boundary Phases in NbFeSb Half-Heusler Alloys: A New Avenue to Tune Transport Properties of Thermoelectric Materials

Ruben Bueno Villoro,* Duncan Zavanelli, Chanwon Jung, Dominique Alexander Mattlat, Raana Hatami Naderloo, Nicolás Pérez, Kornelius Nielsch, Gerald Jeffrey Snyder, Christina Scheu, Ran He,* and Siyuan Zhang*

Many thermoelectric materials benefit from complex microstructures. Grain boundaries (GBs) in nanocrystalline thermoelectrics cause desirable reduction in the thermal conductivity by scattering phonons, but often lead to unwanted loss in the electrical conductivity by scattering charge carriers. Therefore, modifying GBs to suppress their electrical resistivity plays a pivotal role in the enhancement of thermoelectric performance, _zT_. In this work, different characteristics of GB phases in Ti-doped NbFeSb half-Heusler compounds are revealed using a combination of scanning transmission electron microscopy and atom probe tomography. The GB phases adopt a hexagonal close-packed lattice, which is structurally distinct from the half-Heusler grains. Enrichment of Fe is found at GBs in $Nb_{0.95}Ti_{0.05}FeSb$, but accumulation of Ti dopants at GBs in $Nb_{0.80}Ti_{0.20}FeSb$, correlating to the bad and good electrical conductivity of the respective GBs. Such resistive to conductive GB phase transition opens up new design space to decouple the intertwined electronic and phononic transport in thermoelectric materials.

1. Introduction

The worldwide demand for energy has seen consistent increase and is predicted to grow further in the next decades.[1,2] Thermoelectric technology can play an important role in the sustainable economy thanks to the capability to convert heat into electricity and vice versa. By using only solid-state components, thermoelectrics are very attractive for applications such as waste heat recovery[3] and thermal management[4] using devices with scalable sizes. The performance of thermoelectric devices is largely determined by intrinsic transport properties of the materials, which can be evaluated by the dimensionless figure of merit of the materials, $zT = \sigma S^2 T/\kappa$, where σ is the electrical conductivity, S the Seebeck coefficient, T the temperature, and κ the thermal conductivity. Given a certain temperature interval, a higher zT translates to higher conversion efficiency.[5] However, zT enhancement is very challenging to achieve due to the highly intertwined transport of electrons and phonons.[6]

Proposed strategies to improve zT can be classified into two categories: 1) improving the weighted mobility of charge carriers[7] and 2) reducing the lattice thermal conductivity. For the former, approaches such as band convergence,[8–10] modulation doping,[11,12] and resonance levels[13,14] have been successfully employed. For the latter, crystallographic features such as point defects,[15–17] dislocations,[18] stacking faults,[19] grain boundaries (GBs),[20–22] complex unit cells,[23–25] and rattling atoms[26,27] have been demonstrated to reduce the thermal conductivity by enhancing phonon scattering[28] or phonon softening.[29] Among these, one of the most discussed and debated concepts is the study of bulk thermoelectrics with considerably refined grain sizes. The grain refinement can be achieved by rapidly sintering nanograin or amorphous powders from bottom-up (e.g., hydrothermal[30,31]) or top-down (e.g., high-energy ball-milling[32]) synthesis. This strategy is also referred to as "nanostructuring," with the expectation that phonons are more effectively scattered by GBs than electrons, as the former have a much larger and wider dispersion of mean free paths.[33,34] Nanostructuring has been successfully applied to

R. Bueno Villoro, C. Jung, D. A. Mattlat, C. Scheu, S. Zhang
Nanoanalytics and Interfaces
Max-Planck-Institut für Eisenforschung GmbH
Max-Planck-Straße 1, 40237 Düsseldorf, Germany
E-mail: r.bueno@mpie.de; siyuan.zhang@mpie.de
D. Zavanelli, G. J. Snyder
Materials Science & Engineering
Northwestern University
Clark Street 633, Evanston, IL 60208, USA
R. Hatami Naderloo, N. Pérez, K. Nielsch, R. He
Thermoelectric Materials and Devices
IFW Dresden
Helmholtzstraße 20, 01069 Dresden, Germany
E-mail: r.he@ifw-dresden.de

some materials such as Bi_2Te_3,[35,36] BiCuSeO,[37] and SiGe[38,39] to achieve significant reduction of κ while preserving good electrical mobility and hence power factor.

However, recent experimental results have also demonstrated adverse effects of nanostructuring.[40–43] For example, it has been widely reported that in n-type $Mg_3(Sb,Bi)_2$, the electrical conductivity is severely reduced as the grains are refined from micrometer- into nanometer-sized regime.[41,42,44–55] In such cases, GBs cause so much reduction in the electrical conductivity that their beneficial effect in reducing the thermal conductivity is counteracted, causing an overall lower zT. As a result, many thermoelectric materials may behave like $Mg_3(Sb,Bi)_2$ where a sufficient grain size (on the μm order) is necessary for efficient thermoelectrics. GBs are considered as major scattering centers for electrons,[56–61] but not necessarily for phonons until the grain size is sufficiently low.[62]

Phenomenological models have been developed to understand the effect of GBs on the electrical transport. GBs can be considered as potential barriers for charge carriers due to the charge transfer between the GB and the grain, which is referred to as the trapping state model.[58,59] The model has been successfully applied to interpret charge transport mobility limited by the space charge region around GBs. It also predicts that as the doping increases, degenerate semiconductors would have negligible space charge region, so that the GB would no longer limit the mobility.[58] On the other hand, even GBs in metals scatter charge carriers to reduce mobility.[63,64] To formalize their effect in general, Kuo et al. implemented a two-phase model that treats the GB region as a GB phase with an effective conductivity.[47] Such a model can be applied to experimental measurements for both metals and semiconductors, giving the GB phases an effective conductivity. It is important to note that the effective conductivity is not strictly the conductivity of the GB phase itself, rather the averaged contribution to bulk conductivity. In recent years, GB phases, also referred to as GB complexions, have been established into the thermodynamic framework.[65–67] Increasing numbers of GB phases have been discovered, which are shown to have positive[68] or adverse[48] effect on the transport properties.

The general lack of in-depth knowledge of GB phases through atomic-scale characterization is a major obstacle to developing a better understanding of the interaction between GBs and electronic transport. To bridge such a gap, we perform herein an atomic-scale microstructural investigation on GBs using a combination of scanning transmission electron microscopy (STEM), atom probe tomography (APT), and electron back-scattered diffraction (EBSD), and correlate the structural characteristics to the transport properties.

Half-Heusler intermetallic compounds are chosen as they have excellent thermoelectric properties at mid-to-high temperatures, good thermal and mechanical robustness, and elemental components that are earth abundant and benign.[69] In particular, (Nb,V,Ta)FeSb compounds have the highest p-type performance among half-Heusler alloys, due to their very high power factors as a result of d-band convergence in the valence band edge.[70–72] After the initial work on $Nb_{0.4}V_{0.6}FeSb$,[70] Ti-doped NbFeSb attracted more attention since it exhibits high p-type thermoelectric performance[73] and a very large power factor near room temperature.[54] Recently, Ti-doped

NbFeSb-based half-Heusler compounds have been developed into high-efficiency thermoelectric modules that exhibit high power density and conversion efficiency,[74,75] thus, being very interesting for thermoelectric applications. It is found that the thermoelectric properties of Ti-doped NbFeSb display strong correlation to the GBs.[42,54] The $Nb_{0.95}Ti_{0.05}FeSb$ material has one of the highest power factors among all thermoelectric materials, exceeding 100 μW cm^{-1} K^{-2}.[54] Interestingly, such high electrical conductivity is only realized in coarse-grained materials with little presence of GBs. On the other hand, $Nb_{0.80}Ti_{0.20}FeSb$ shows completely different behaviors, where the grain size has little impact on the electrical conductivity. This puzzling behavior was discussed in a recent review by Hu et al.,[76] who attributed the lack of grain size dependence to the higher carrier concentration in $Nb_{0.80}Ti_{0.20}FeSb$. The GB phases are considered as the same, but the charge carrier depletion region decreases due to higher doping, which causes less charge carrier scattering by GBs. It is also noteworthy that the size of the space charge region depends on the different carrier density between the bulk and the GBs, so that the structure and composition of the GB phase would also play a determining role.

In this article, we report different GB phases found in NbFeSb alloys with different Ti doping concentrations, which offers a complementary explanation to their different transport properties with grain size. The resistive (low Ti doping) to conductive (high Ti doping) GB phase transition was found to be caused by the compositional transition from Fe-rich to Ti-rich GB phases. After finding out the hexagonal close-packed (HCP) structure of the GB phases, they can be well distinguished from the face centered cubic (FCC) matrix phase so that their lattice structures can be determined. Such detailed knowledge on the GB phases enables the understanding of the resistive to conductive GB phase transition. The transition towards electrically conductive GB phases enables a new avenue to optimize thermoelectric performance, as the electronic and phononic transport can be effectively decoupled.

2. Results and Discussion

2.1. Tuning the Grain Size

Ti is one of the best p-type dopants in NbFeSb by substituting the Nb site.[54] 5% Ti is sufficient to reach a high power factor, but close to 20% Ti was required to reduce the thermal conductivity that led to the best zT values for NbFeSb at high temperatures.[54] To understand the apparent discrepancy, we synthesized both compositions $Nb_{0.95}Ti_{0.05}FeSb$ and $Nb_{0.80}Ti_{0.20}FeSb$ by powder metallurgy routes. To study the effect of GBs in both alloys, the powders have been sintered at 1123 and 1273 K, to reach smaller and larger grain sizes, respectively. As evidenced by the X-ray diffraction (XRD) patterns shown in Figure S1a,b, Supporting Information, half-Heusler is the only dominant phase in all samples. Moreover, the lattice parameters of $Nb_{0.95}Ti_{0.05}FeSb$ sintered at 1123 and 1273 K (0.595(1) nm and 0.595(2) nm) and $Nb_{0.80}Ti_{0.20}FeSb$ 1123 and 1273 K (0.595(4) nm and 0.595(3) nm) are in good agreement with literature values (0.5947 nm for $Nb_{0.96}Ti_{0.04}FeSb$ and 0.594(0) nm for $Nb_{0.80}Ti_{0.20}FeSb$[73]). There is negligible
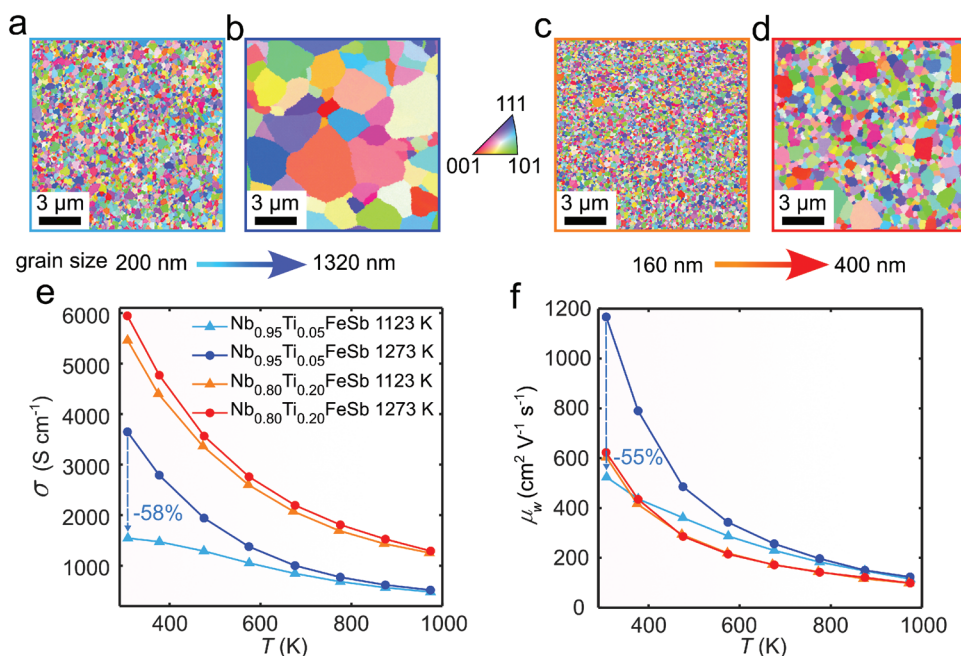
Figure 1. Effect of the grain size on the electrical transport. The grain size (GS) is tuned by the sintering temperatures, shown in EBSD maps of $Nb_{0.95}Ti_{0.05}FeSb$ samples sintered at a) 1123 K and b) 1273 K and $Nb_{0.80}Ti_{0.20}FeSb$ samples sintered at c) 1123 K and d) 1273 K. e) Electrical conductivity σ and f) weighted mobility μ_w are hardly affected by different grain sizes of $Nb_{0.80}Ti_{0.20}FeSb$, but they are significantly reduced in fine-grained $Nb_{0.95}Ti_{0.05}FeSb$.

difference in lattice parameters for samples with the same composition sintered at different temperatures or with different Ti doping. All four samples have a 99% density with respect to the theoretical values, and hence a similar porosity of 1%. Small numbers of pores can be found in the SEM and STEM images (Figures S2 and S3, Supporting Information), where the samples show very different grain sizes.

As shown in **Figure 1**a–d, both samples sintered at 1123 K have an ultrafine grain size of ≈200 nm while at the higher sintering temperature of 1273 K, $Nb_{0.95}Ti_{0.05}FeSb$ reaches >1 µm grain size, whereas $Nb_{0.80}Ti_{0.20}FeSb$ grew to ≈400 nm. Figure S4, Supporting Information, further shows that the grain size of each sample follows the log-normal distribution and the misorientation angle of GBs fits well to the random Mackenzie[77] distribution.

2.2. Effect of Grain Size on the Thermoelectric Properties

The electrical and thermal transport properties of all samples were measured and plotted in Figure 1e,f and Figure S5, Supporting Information. In particular, the electrical conductivity is very sensitive to the different doping concentrations and grain sizes. As shown in Figure 1e, the near room temperature (307 K) electrical conductivity of fine-grained $Nb_{0.95}Ti_{0.05}FeSb$ is 58% lower than its coarse-grained counterpart. In contrast, the conductivity of fine-grained $Nb_{0.80}Ti_{0.20}FeSb$ is only reduced by 8% in comparison to the coarse-grained sample. A lower conductivity can be caused by either reduced carrier concentration (n) or mobility (μ) (following $\sigma = ne\mu$ where e is the elementary charge). The Hall measurements confirm that the carrier

concentration has little dependence on the grain size and is ≈3 times higher in $Nb_{0.80}Ti_{0.20}FeSb$ (2.9–3.0 × 10^{21} cm^{-3}) than in $Nb_{0.95}Ti_{0.05}FeSb$ (9.8 × 10^{20} cm^{-3}). Therefore, the lowered conductivity of the fine-grained $Nb_{0.95}Ti_{0.05}FeSb$ sample is due to reduced carrier mobility. Here we utilize the weighted mobility (μ_w),[78] instead of the apparent Hall mobility, across the whole temperature range to better apprehend the electronic transport properties imposed by the band complexity. As shown in Figure 1f, the weighted mobility shows a strong dependence on the grain size for $Nb_{0.95}Ti_{0.05}FeSb$ (55% reduction at near room temperature from coarse- to fine-grained samples), but nearly identical for $Nb_{0.80}Ti_{0.20}FeSb$ samples regardless of the grain size (3% reduction from coarse- to fine-grained). It has also been shown in literature[79] that the mobility of $Nb_{0.80}Ti_{0.20}FeSb$ stays similar at increased grain size of 0.8–1.6 µm.

The contrasting trends can be further understood by different mechanisms for the scattering of charge carriers. The most common type of electron scattering is by acoustic phonons, which would lead to a decreasing mobility (and hence conductivity) upon heating following $T^{-3/2}$.[80] Indeed, as shown in supplemental Figure 6, the $T^{-3/2}$ trend is followed by both $Nb_{0.80}Ti_{0.20}FeSb$ samples and the coarse-grained $Nb_{0.95}Ti_{0.05}FeSb$ sample, confirming that the scattering of charge carriers in these three samples is dominated by acoustic phonons, showing a metallic behavior. In contrast, the fine-grained $Nb_{0.95}Ti_{0.05}FeSb$ sample displays a significant deviation from the metallic behavior, reveals a major reduction in μ_w at lower temperatures, which indicates the dominance of other scattering mechanisms. Considering the ultrafine grain size (and consequently higher proportion of GBs) is the major difference of the sample,
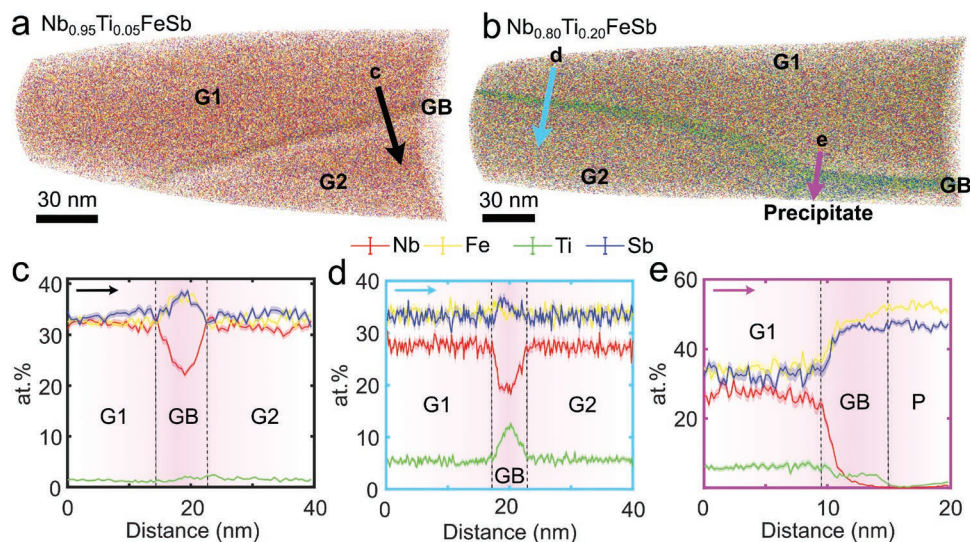
Figure 2. Atomic compositions at the GBs. APT 3D reconstructions of a) $Nb_{0.95}Ti_{0.05}FeSb$ and b) $Nb_{0.80}Ti_{0.20}FeSb$ sintered at 1273 K show chemical changes at the GBs. c) The composition line profile along the G1–GB–G2 region (black arrow in (a)) shows Nb depletion enrichment in Sb and Fe. d) The line profile along the G1–GB–G2 region (cyan arrow in (b)) shows Nb depletion and enrichment in Sb and Ti. e) The line profile along the G1–GB–P boundary (magenta arrow in (b)) shows a $Fe_{1+x}Sb$ precipitate and a Ti-enriched phase boundary. The cylinder diameter is 20 nm for all line profiles.

electron scattering by GBs is determined as the dominant scattering mechanism in fine-grained $Nb_{0.95}Ti_{0.05}FeSb$. As the GB scattering term does not follow the same temperature dependence, this is consistent with the major discrepancy from the electron–phonon $T^{-3/2}$ trend (metallic behavior) at lower temperatures. The GB-dominated electron scattering has been reported in many fine-grained thermoelectric materials, including Mg_3Sb_2,[52] $ZrCoSb$,[42] $NbCoSn$,[81] $GeTe$,[68] and $TiCoSb$.[82] At larger grain sizes (>1 µm), the GBs are sufficiently far apart so that their contribution to the scattering term becomes negligible. Nevertheless, this would also rule out major contribution of GBs in phonon scattering and close down the design space of nanostructuring in thermoelectrics.

Although electron-GB scattering may rationalize the reduced mobility of fine-grained $Nb_{0.95}Ti_{0.05}FeSb$, it is perplexing that the same mechanism does not apply to $Nb_{0.80}Ti_{0.20}FeSb$, which has even smaller grain sizes and hence more GBs. One possible explanation is that GBs in different samples are also different in terms of composition or atomic arrangement, which would hence lead to different transport properties. Based on the electrical measurements, we hypothesize that the GBs of $Nb_{0.95}Ti_{0.05}FeSb$ are electrically resistive, whereas GBs in $Nb_{0.80}Ti_{0.20}FeSb$ are not. This would allow for the same interpretation of electron-GB scattering in both fine-grained samples (i.e., sintered at 1123 K) but with different transport behaviors as discussed above. Such a hypothesis, if validated, may have a profound impact in optimizing thermoelectric materials since nanostructuring will become a viable solution again, provided that the GB resistance can be drastically reduced. However, there is little understanding on how the variation of the GB structure and chemistry impact on the scattering of charge carriers to our knowledge. Being able to modify the transport properties of GBs would open up new opportunities to decouple the optimization of electrical and thermal transport in thermoelectrics.

2.3. Compositional Variation at GBs

To test our hypothesis on the transition of GB properties, we look into the chemical composition of the GBs by APT and energy dispersive X-ray spectroscopy (EDS) performed in a STEM.

Figure 2a,b shows the respective APT 3D reconstruction of $Nb_{0.95}Ti_{0.05}FeSb$ and $Nb_{0.80}Ti_{0.20}FeSb$ samples, each sampling over two grains G1 and G2 and the GBs in between. The line profiles across the GBs clearly evidence the changes in chemical compositions with respect to the neighboring grains. The GB in $Nb_{0.95}Ti_{0.05}FeSb$ is depleted in Nb and enriched in Sb and Fe (Figure 2c). On the other hand, the GB in $Nb_{0.80}Ti_{0.20}FeSb$ also has Nb depletion and Sb enrichment, but Ti is enriched at the GB instead of Fe (Figure 2d, see also the Video S1, Supporting Information).

To confirm the segregation behavior of GBs in different samples, several GBs across multiple APT tips and TEM samples have been sampled (more APT datasets are shown in Figure S7, Supporting Information). The same phenomenon is also observed by STEM-EDX for all four samples. While the GBs in fine- and coarse-grained $Nb_{0.95}Ti_{0.05}FeSb$ show enrichment in Fe (Figure S8, Supporting Information), the GBs in fine- and coarse-grained $Nb_{0.80}Ti_{0.20}FeSb$ are enriched in Ti instead (Figure S9, Supporting Information). Such a difference in the chemical compositions of GBs in $Nb_{0.95}Ti_{0.05}FeSb$ and $Nb_{0.80}Ti_{0.20}FeSb$ provide a good hint toward their different conductive behavior.

2.4. Atomic Configuration of the GB Phases

To further our understanding on the defect phases, the atomistic structures of the GB phases were revealed using high angle annular dark field (HAADF)-STEM imaging. As shown
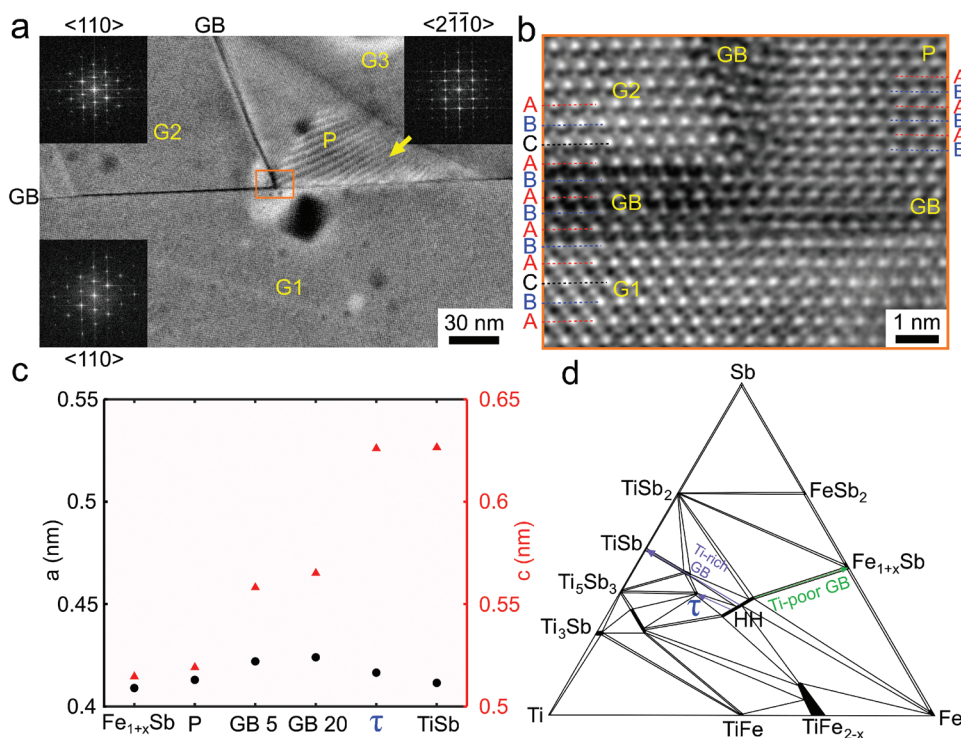
Figure 3. Atomic arrangement of the GB phases. a) HAADF-STEM images taken in $Nb_{0.80}Ti_{0.20}FeSb$ show two grains (G1 and G2) in $\langle 110 \rangle$ zone axis and one precipitate (P) in $\langle 2\bar{1}\bar{1}0 \rangle$ zone axis. The GB phase is visible at all boundaries. b) A magnified section at the triple point present the atomic stacking for G1, G2, P, and the three boundaries. The stacking of the GB and P phases follow the HCP structure (AB), while G1 and G2 have the FCC stacking order (ABC). c) a and c lattice parameters are measured for $Nb_{0.95}Ti_{0.05}FeSb$ (GB 5) and $Nb_{0.80}Ti_{0.20}FeSb$ (GB 20) samples and compared with the precipitate (P) (shown in (b)) and literature values for $Fe_{1+x}Sb$,[83] $TiSb$[84] and $Ti_{1.18}Fe_{0.57}Sb$.[85] d) The isothermal section (1070 K) of the ternary Ti–Fe–Sb phase diagram (redrawn based on ref. [85]) highlighting the half-Heusler (HH) TiFeSb phase in the center, the $Fe_{1+x}Sb$ phase in the Ti-poor, as well as TiSb and the τ phase $Ti_{1.18}Fe_{0.57}Sb$ close to the Ti-rich side.

in **Figure 3**a, the GB phases between the half-Heusler grains G1, G2, and G3 as well as the precipitate P are continuous and have a darker HAADF contrast. To reveal the atomic structure of half-Heusler compounds, it is convenient to image along the <110> zone axis, where all three atomic sites (Nb/Ti, Fe, Sb) are separated and their stacking order can be resolved. As shown in Figure 3b, the FCC ABC stacking of (111) planes is revealed inside the half-Heusler grains. However, the GB between G1 and G2 shows the AB stacking order, in agreement with HCP crystals. To understand the atomic arrangement at the GB, we notice their similarity to the HCP structure of the $Fe_{1+x}Sb$ phase. $Fe_{1+x}Sb$ crystallizes in the NiAs-type $P6_3/mmc$ structure and the excess Fe atoms ($0.08 < x < 0.38$) occupy the interstitial positions.[83] Such precipitate is captured in Figure 3a,b and labeled as P. An orientation relationship exists between P and the half-Heusler grains, $[2\bar{1}\bar{1}0]_P // [1\bar{1}0]_{G1}$ and $(0001)_P // (111)_{G1}$. The $Fe_{1+x}Sb$ phase has also been found and analyzed using APT, as presented in Figure 2e and Video S1, Supporting Information. The composition was determined as $Fe_{1.11}Sb$, with very limited solubility of Ti (0.8%) and Nb (0.2%). Having the same structure as the $Fe_{1+x}Sb$ precipitate, it is not straightforward whether to describe the GB as an individual defect phase, or simply a bulk phase precipitated at the GB. To resolve the puzzle, we further examined the lattice parameters and compositions of the precipitate and the GB phase. The a and c lattice parameters are measured by the interplanar distances between

$(10\bar{1}0)$ and (0002) planes, respectively, as shown in Figure S10, Supporting Information. It is evident that although the a lattice parameters of the GB phase and the precipitate are close, their c lattice parameters deviate by >10 % (Figure 3c). Furthermore, according to the APT line profile (Figure 2e), the composition across from G1 to P does not show an abrupt change. Instead, a transition region was found in between with higher Ti content with respect to the $Fe_{1+x}Sb$ precipitate. These are strong evidences for a coherent GB phase with limited thickness (several nm), but nevertheless distinct lattice parameters and compositions. Based on the experimental results, we propose the presence of a GB phase with HCP structure sandwiched between two FCC half-Heusler NbFeSb grains. In addition to $Fe_{1+x}Sb$,[83] we found two more intermetallic phases in the Ti-Fe-Sb system (Figure 3d) that crystallize in the HCP structure, TiSb[84] and the ternary τ-phase $Ti_{1.16}Fe_{0.57}Sb$.[85] All three phases are listed in Figure 3c to compare their a and c lattice parameters with the experimental values from the $Fe_{1+x}Sb$ precipitate and two GB phases found at $Nb_{0.95}Ti_{0.05}FeSb$ (GB 5) and $Nb_{0.80}Ti_{0.20}FeSb$ (GB 20). The GB phases have a slightly increased a parameter with respect to $Fe_{1+x}Sb$, TiSb, and the τ-phase. Indeed, as the GB phase is coherent with the half-Heusler matrix, the a direction in the GB phase is also constrained to the 1/2[110] direction of the half-Heusler phase, which has a length of 0.421 nm. There are bigger differences between the c lattice parameters of $Fe_{1+x}Sb$ (0.515 nm),[83] the τ-phase (0.626 nm)[85] and TiSb

(0.626 nm).[84] The GB phases have intermediate values of 0.558 nm and 0.565 nm for $Nb_{0.95}Ti_{0.05}FeSb$ (GB 5) and $Nb_{0.80}Ti_{0.20}FeSb$ (GB 20), respectively.

The APT results presented in Figure 2c have shown that the GBs in $Nb_{0.95}Ti_{0.05}FeSb$ are Ti poor. Therefore, the GB5 phase is likely similar to $Fe_{1+x}Sb$. On the other hand, the GBs in $Nb_{0.80}Ti_{0.20}FeSb$ are Ti rich, so that the GB20 phase would locate closer to the Ti-rich (left) corner of the phase diagram, being more similar to the τ and TiSb phases.

2.5. Composition and Site Occupation of the GB Phases

To determine the chemical composition of the GB phases, we notice that the GBs are so thin (1–2 nm) that they reach the resolution limits of various microanalysis techniques. For APT, broadening of segregation profiles is commonly observed at GBs due to their different field evaporation behavior (more in Figure S11, Supporting Information).[86,87] For EDX, the broadening is caused by the propagation of STEM probe across the sample thickness, especially electrons scattered to high angles.[88] To characterize the segregation behavior independent to the broadening effects, we apply an integrated quantity, the Gibbsian interfacial excess[89] (Γ). For example, the Nb composition profile across the GB in **Figure 4**a spans to ≈ 5 nm, whereas the width of the GB phase is only 1.7 nm (Figure 3b). The Nb composition in the half-Heusler phase is well known, summing to 1/3 with the doping concentrations of Ti (**Figure 5**b,d). Moreover, Nb is not a component of the ternary TiFeSb phases (Figure 3d) and hence has a nominal composition of 0 inside the defect phases. Based on the concentration and the thickness of the GB phase, we can model the composition profile of Nb (Nb model profile) to compare with the Nb APT profile. As shown in Figure 4a, both profiles lead to very similar $\Gamma(Nb)$ (shaded areas), -26 Nb atoms nm^{-2} (negative numbers indicate depletion at GBs). This result suggests that Γ is a reliable quantity to characterize the segregation behavior.

As shown in Equation (1), Γ scales linearly with the thickness of the GB phase, t, as well as the difference in the atomic density of element i between the matrix and the GB phases, $\Delta\rho_i$.

$$\Gamma_i = t \times \Delta\rho_i = t \times \left(\frac{N_i^{GB}}{V_{GB}} - \frac{N_i^{G}}{V_G} \right) \qquad (1)$$

where N_i^G and N_i^{GB} are the number of atoms of element i in the respective unit cells of the half Heusler grain (G) and the GB phase, V_G and V_{GB} are the unit cell volumes of the respective phases.

By assuming no Nb inside the GB phases $N_{Nb}^{GB} = 0$, the required thicknesses to reach the Γ_{Nb} values observed in $Nb_{0.95}Ti_{0.05}FeSb$ and $Nb_{0.80}Ti_{0.20}FeSb$ are evaluated as 1.46 and 1.74 nm, respectively. As shown in Figure 4b, they are in good agreement with the experimentally observed thickness of the GB phases in the respective samples. The analysis hence supports a structural model of GB phases free of Nb and of the experimentally observed thicknesses in the STEM images. As plotted in Figure 4c, GBs in both $Nb_{0.95}Ti_{0.05}FeSb$ and $Nb_{0.80}Ti_{0.20}FeSb$ have comparable excess values for Nb depletion and Sb enrichment, but show major differences in Γ_{Ti} and Γ_{Fe}. GBs in $Nb_{0.95}Ti_{0.05}FeSb$ are enriched in Fe, but have little excess in Ti. In contrast, GBs in $Nb_{0.80}Ti_{0.20}FeSb$ are enriched in Ti, but have negligible excess in Fe.

To model the structure of GB phases with confined thickness and HCP structure, it is critical to reveal the occupation of their crystal sites by Ti, Fe, and Sb. By applying the Γ_{Ti}, Γ_{Fe}, and Γ_{Sb} (Figure 4c) as well as the thickness (Figure 4b) into Equation (1), we can evaluate the atomic density of the respective elements inside the GB phases. As shown in Figure 5, the atomic composition of the GB phases in $Nb_{0.95}Ti_{0.05}FeSb$ and $Nb_{0.80}Ti_{0.20}FeSb$ are determined as $(Ti_{0.07},Fe_{1.03})Sb$ (Figure 5c) and $(Ti_{0.63},Fe_{0.77})Sb$ (Figure 5d); respectively. The derived compositions have a relative surplus of Fe + Ti with respect to Sb, corresponding to $x = 0.1, 0.4$ in the formula $(Ti,Fe)_{1+x}Sb$. As reported by Yamaguchi et al.,[83] a surplus of Fe is necessary to stabilize the HCP $Fe_{1+x}Sb$ phase ($0.08 < x < 0.38$). We hence allocate Sb to the 2c sites of the HCP phase, whereas Ti and Fe occupy the 2a and interstitial sites. The two GB phases are fully represented in the HAADF-STEM images (Figure 5a,c). Among all elements in the samples, Sb has the highest atomic number and hence the brightest HAADF contrast, as they occupy the 4b sites in the half Heusler matrix and the 2c sites in the GB phases. Nb atoms have the second highest contrast and can be
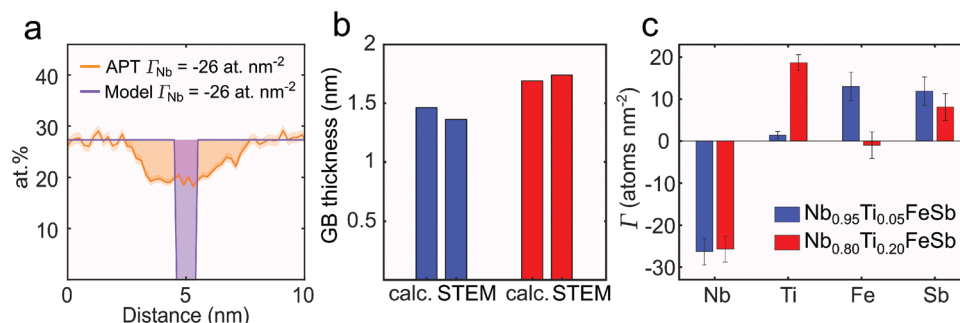
Figure 4. Connecting the segregation at GBs to their thickness using Gibbsian interfacial excess Γ. a) The APT line profile of Nb composition (orange, reproduced from Figure 2d) is compared to a step function with 0 at.% of Nb in the GB phase and a width corresponding to the GB thickness observed in STEM between the Nb composition in the grain (purple (Model)), both showing similar Γ_{Nb}. b) Good agreement is found between the GB thicknesses observed in STEM and the calculated values based on Γ_{Nb} (calc.). c) Γ values determined for all four elements in the GB phases of $Nb_{0.95}Ti_{0.05}FeSb$ (blue) and $Nb_{0.80}Ti_{0.20}FeSb$ (red).
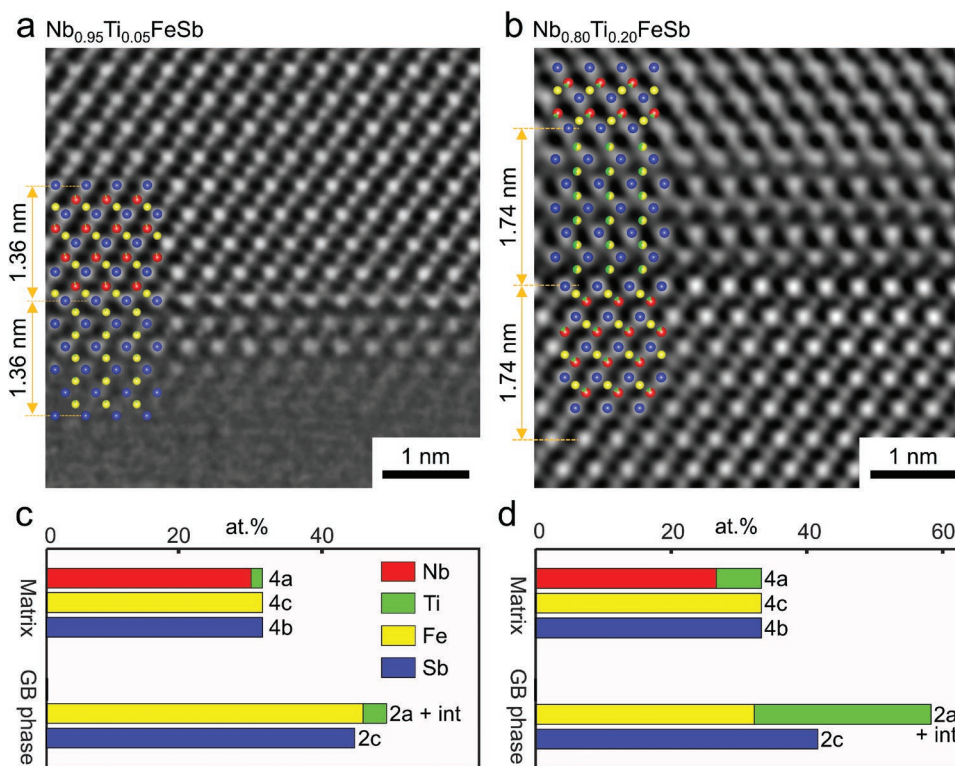
Figure 5. GB phases identified in $Nb_{0.95}Ti_{0.05}FeSb$ and $Nb_{0.80}Ti_{0.20}FeSb$. a,b) HAADF-STEM images of respective samples sintered at 1273 K with over-laid atomic arrangements and c,d) the respective atomic site occupation in the half-Heusler matrix and the GB phases.

identified on the 4a sites in the matrix and absent in the GB phases. Fe and Ti can also be observed on the 2a sites of the GB phases, while Fe in the matrix 4c sites are largely overshadowed by the neighboring atomic columns.

2.6. Electrical Properties of the GB Phases

Having determined the different GB phases in the two alloys, we continue to rationalize their distinctive effects on the electrical transport. To highlight the contribution of GB phases, we apply a two phase model[47] to separate the electrical transport through the grain interior (σ_G) and the GBs (σ_{GB}).

$$\sigma^{-1} = (1 - f_{GB})\sigma_G^{-1} + f_{GB}\sigma_{GB}^{-1} \qquad (2)$$

where the volume fraction of the GB phase $f_{GB} = L_{EBSD} \times t_{GB}/A_{EBSD}$ can be evaluated by the ratio between the area of the GB phase (total length L_{EBSD} multiplies with the GB thickness t_{GB} in Figure 4c) and the area of the respective EBSD scans A_{EBSD} (Figure 1a–d). f_{GB} is determined as 2.0% and 0.2% for $Nb_{0.95}Ti_{0.05}FeSb$ samples sintered at 1123 and 1273 K, 3.3% and 1.0% for $Nb_{0.80}Ti_{0.20}FeSb$ samples sintered at 1123 and 1273 K, respectively.

Applying the 2-phase model to each fine/coarse-grained pair, electrical transport through the grain interior (σ_G, **Figure 6**a) shows the same temperature dependence ($T^{-3/2}$), while the alloy with higher doping concentration $Nb_{0.80}Ti_{0.20}FeSb$ also exhibits higher conductivity. In contrast, the transport properties of the GB phases are fundamentally different (σ_{GB}, Figure 6b). While the GB phase in $Nb_{0.80}Ti_{0.20}FeSb$ behaves like a metal (conductivity following the $T^{-3/2}$ trend), the GB phase
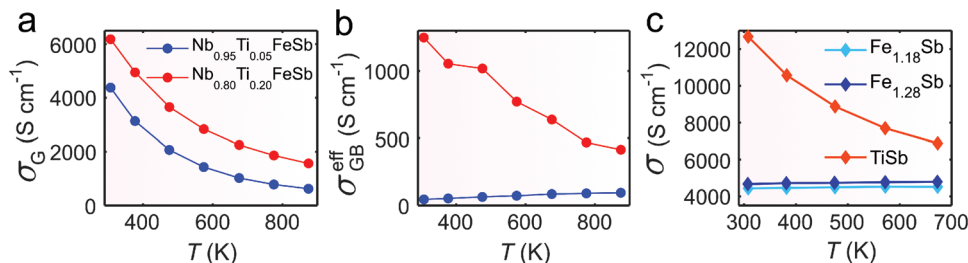
Figure 6. GB phases of $Nb_{0.80}Ti_{0.20}FeSb$ present a metallic behavior while GB phases of $Nb_{0.95}Ti_{0.05}FeSb$ are non-metallic. Using the two phase model a) σ_G and b) σ_{GB} are calculated. c) Bulk phases of TiSb, $Fe_{1.18}Sb$, and $Fe_{1.28}Sb$ are measured presenting non-metallic temperature dependent behavior for $Fe_{1+x}Sb$ and metallic behavior for TiSb.

**ADVANCED
SCIENCE NEWS**

www.advancedsciencenews.com

**ADVANCED
ENERGY
MATERIALS**

www.advenergymat.de

in $Nb_{0.95}Ti_{0.05}FeSb$ has remarkably lower conductivity and clearly lost the metallic behavior.

To further understand how the compositional variation of the GB phases changes the electrical conductivity, we synthesized samples with compositions close to the $Fe_{1+x}Sb$ precipitate ($Fe_{1.18}Sb$ and $Fe_{1.28}Sb$), TiSb, as well as compositions corresponding to both GB phases. The attempts to synthesize the bulk form of the two GB phases were not successful, as the samples show phase separation according to the ternary phase diagram (Figure 3d). This further proves that the observed GB phases are only stabilized by their confined thickness dimension as well as the interface with the half-Heusler matrix, a typical observation for complexions.

Single-phase samples were successfully synthesized for the three compositions, $Fe_{1.18}Sb$, $Fe_{1.28}Sb$, and TiSb (see Figure S12, Supporting Information), so that their electrical conductivity can be measured in the bulk. As shown in Figure 6c, TiSb has the highest electrical conductivity and also exhibits a metallic behavior ($T^{-3/2}$ trend). The other two compounds, $Fe_{1.18}Sb$ and $Fe_{1.28}Sb$, have similarly low electrical conductivity, so that the amount of interstitial Fe atoms does not significantly change the electrical transport. Moreover, both Ti-free compounds have almost constant electrical conductivity in the measured temperature range, in stark contrast to the metallic behavior of TiSb.

Comparing the transport properties between GB and the bulk phases is never straightforward. For example, the $Fe_{1+x}Sb$ phases, although more resistive than TiSb, still have comparable conductivity to the half-Heusler matrix. On one hand, the compositions and lattice parameters observed in the GB phases can not be stabilized in the bulk. There are also phases such as $FeSb_2$ that have significantly worse conductivity.[90] On the other hand, the two phase model assumes a series circuit configuration for a resistive GB in a conductive grain, representing an effective GB resistivity rather than its physical magnitude as bulk phases. Nevertheless, we observe some similarity in the temperature dependence of various electrical conductivity curves plotted in Figure 6. In particular, the almost constant $Fe_{1.18}Sb$ and $Fe_{1.28}Sb$ curves with respect to the temperature (Figure 6c) corresponds well to the non-metallic behavior of the Ti-poor GB phase in $Nb_{0.95}Ti_{0.05}FeSb$ (Figure 6b). Moreover, the $T^{-3/2}$ trend of TiSb (Figure 6c) correlates well to the metallic behavior of the Ti-rich GB phase in $Nb_{0.80}Ti_{0.20}FeSb$ (Figure 6b). The observed trends support our hypothesis that the enhanced Ti content in the GB phase leads to significant improvement of the GB conductivity.

Last but not least, it is also reported that the diminishing thickness of the charge depletion layer by increasing doping concentration would lead to less GB scattering.[76] Nevertheless, we note that the charge carrier concentration is already so high for the low doping sample $Nb_{0.95}Ti_{0.05}FeSb$, 10^{21} cm^{-3}, that the depletion layer would be too thin to model.[58] For example, we take the guide from Seto[59] to evaluate the GB energy barrier from the charge trapping model, and found all four samples, including the lower doping $Nb_{0.95}Ti_{0.05}FeSb$, to have negative energy barriers. This can be understood from the negative slopes in the σ versus T plot in Figure 1e, which would lead to negative slopes in the $\ln(\sigma)$ versus $-1/kT$ plot, which are proportional to the energy barriers.

Therefore, GBs should not be simply considered as defects that impede the transport of charge carriers, but rather they can be treated as phases and tuned towards higher conductivity. Accordingly, we propose a new avenue to tune the transport properties of thermoelectric materials: Constructing thermoelectric materials with significantly refined grain sizes down to sub-micrometer level to suppress phonon transport, meanwhile maintaining high power factor by tuning the GB phase toward high electrical conductivity. Further design of GB phases can be explored by either changing the composition of the native matrix phase, as discussed in this work, or introducing foreign 2D phases such as graphene[91] and nanometer-thick ZnO by atomic layer deposition.[92,93]

3. Conclusion

In this work, we have discovered GB phases in the half-Heusler NbFeSb alloys with p-type Ti doping. These phases are present homogeneously along the GBs, with a thickness of 1–2 nm. Unlike the FCC matrix phase, the GB phases have the HCP stacking order and little content of Nb. Although structurally similar to the bulk phases $Fe_{1+x}Sb$ and TiSb, the GB phases have compositions that are subject to phase separation in the bulk, and distinctive lattice parameters matched in-plane to the half-Heusler matrix. We demonstrate that depending on the Ti content in the matrix, the GB phase can be tuned to be either enriched in Fe or Ti. The Fe-rich GB phase is observed in $Nb_{0.95}Ti_{0.05}FeSb$, which also suffers from significant reduction in the electrical conductivity with increasing fraction of GBs (nanostructuring). The resistive nature of this GB phase is comparable to a similar bulk phase $Fe_{1+x}Sb$. On the other hand, by introducing more Ti, the GB phase in $Nb_{0.80}Ti_{0.20}FeSb$ becomes Ti rich and exhibits metal-like conductive behavior, comparable to the bulk phase TiSb. As a result, the electrical conductivity of $Nb_{0.80}Ti_{0.20}FeSb$ no longer shows a dependence on the grain size. Our results have proven the concept that the electrical transport can be tuned by resistive to conductive GB phase transition, providing an alternative solution to decouple the electrical and thermal transport in nanostructured thermoelectric materials. The design of GB phases requires detailed atomic-scale characterization, and this work sets a solid foundation for the determination of the crystal structure, composition, and site occupation of GB phases to correlate with their transport properties. Future designs on the GB phases can offer expanded space to improve the transport properties of thermoelectrics and other functional materials.

4. Experimental Section

Synthesis: The half-Heusler materials with nominal compositions of $Nb_{0.95}Ti_{0.05}FeSb$ and $Nb_{0.80}Ti_{0.20}FeSb$ were prepared through a solid-state synthesis. In total 10 g of raw elements, including Nb powders (99.8%, Alfa Aesar), Fe granules (99.98%, Alfa Aesar), Ti sponges (99.95%, Alfa Aesar), and Sb pieces (99.999%, MaTecK), were weighted according to the stoichiometry and loaded into ball milling jars with O_2 and H_2O level lower than 2 ppm. The weighed raw elements were ball milled for 14 h by a SPEX 8000D machine using hardened steel vials and two 12 mm stainless steel balls with powder loosing on the 5th, the 10th, and the 12th hour. The ball-milled powders were compacted using a field-assisted sintering technique (FAST, FCT Systeme GmbH) under 50 MPa for 5 min at 1123 or 1273 K. The sintering was carried out under vacuum.

The sintered compounds were cut and polished to the desired sizes for measuring the transport properties.

Property Measurement: The electrical conductivity (σ) and the Seebeck coefficient (S) were measured using a commercial device LSR-3 (Linseis). The thermal conductivity (κ) was calculated as a multiplication of thermal diffusivity (D), specific heat (C_p), and mass density (d). The thermal diffusivity and the mass density were measured by laserflash (LFA1000, Linseis) and an Archimedes kit, respectively. The specific heat takes the literature value of He et al.[54] The measurement errors were 4%, 5%, and 12% for σ, S, and κ, respectively. Explicitly, the uncertainties of κ originated from 2% in mass density, 4% in diffusivity, and 6% in specific heat. Therefore, the uncertainties in power factor and zT were 10% and 20%, respectively. To increase the readability of the graphs, the error bars were not added on the curves. The Wiedemann–Franz law was used to calculate κ_e and obtain κ_l as shown in Equation (3):

$$\kappa_l = \kappa - L\sigma T \tag{3}$$

where L is the Lorenz factor calculated as shown by Kim et al.[94]

Microstructure Characterization: Solid XRD of all samples was performed on polished surfaces using a diffractometer Riaku Smartlab 9KW with a Cu K$_\alpha$ source ($\lambda = 0.154059$ nm). Lattice parameters were calculated using the Bragg's law on the ten main peaks of the XRD. The reference peaks were calculated using Vesta[95] with the experimental lattice parameters.

Samples were prepared for SEM investigation using SiC papers for grinding and diamond and OPS suspension solutions for polishing. SEM characterization was performed in a Sigma 500 Zeiss microscope operated at 15 kV. EBSD was acquired at 15 kV, 10 nA and a working distance of 20 mm using a EDAX/TSL system with a Hikari camera.

Specimens for STEM investigation were prepared using a Scios2 (Thermo Fisher) focused ion beam (FIB). A general procedure described by Schaffer et al.[96] has been used for lamella preparation. Specimens were thinned down to <150 nm by 30 keV Ga$^+$ beam, and final thinning and cleaning were performed at 5 and 2 kV.

The STEM characterization was performed in a Titan Themis probe-corrected microscope operated at 300 kV. The collection semiangle of 24 mrad and ≈0.1 nm probe size was used. HAADF-STEM images were acquired using a collection angle of 73–200 mrad. To reduce noise in the images, 25–30 frames are averaged with a pixel dwell time of 1–2 μs each frame. STEM-EDX maps were acquired using a four-quadrant silicon-drift EDX detector (Super-X) in ≈30 min acquisition time for each map. Multivariate statistical analysis was performed for noise reduction and the Cliff–Lorimer formula was used for elemental quantification.[97]

The Scios2 FIB (Thermo Fisher) was also used to fabricate APT specimens using a procedure described by Thompson et al.[98] APT experiments were performed using a local electrode atom probe (CAMECA LEAP 5000 XR) in pulsed laser mode at a specimen base temperature of ≈60 K and detection rate of 1%. The laser pulse energy and frequency were set to 30 pJ and 125 kHz, respectively. Data reconstruction and analyses were done with AP suite 6.1 software, provided by CAMECA Instruments. Γ values were calculated by using a ladder diagram.[89]

Supporting Information

Supporting Information is available from the Wiley Online Library or from the author.

Acknowledgements

Conflict of Interest

The authors declare no conflict of interest.

Data Availability Statement

The data that support the findings of this study are available in the supplementary material of this article.

Keywords

[1] T. Kober, H.-W. Schiffer, M. Densing, E. Panos, *Energy Strategy Rev.* **2020**, *31*, 100523.

[2] K. Kaygusuz, *Renewable Sustainable Energy Rev.* **2012**, *16*, 1116.

[3] S. LeBlanc, *Sustainable Mater. Technol.* **2014**, *1–2*, 26.

[4] G. Li, J. Garcia Fernandez, D. A. Lara Ramos, V. Barati, N. Pérez, I. Soldatov, H. Reith, G. Schierning, K. Nielsch, *Nat. Electron.* **2018**, *1*, 555.

[5] G. J. Snyder, A. H. Snyder, *Energy Environ. Sci.* **2017**, *10*, 2280.

[6] G. J. Snyder, E. S. Toberer, *Nat. Mater.* **2008**, *7*, 105.

[7] X. Zhang, Z. Bu, X. Shi, Z. Chen, S. Lin, B. Shan, M. Wood, A. H. Snyder, L. Chen, G. J. Snyder, Y. Pei, *Sci. Adv.* **2022**, *6*, eabc0726.

[8] W. Liu, X. Tan, K. Yin, H. Liu, X. Tang, J. Shi, Q. Zhang, C. Uher, *Phys. Rev. Lett.* **2012**, *108*, 166601.

[9] H. Zhu, R. He, J. Mao, Q. Zhu, C. Li, J. Sun, W. Ren, Y. Wang, Z. Liu, Z. Tang, A. Sotnikov, Z. Wang, D. Broido, D. J. Singh, G. Chen, K. Nielsch, Z. Ren, *Nat. Commun.* **2018**, *9*, 2497.

[10] Y. Pei, X. Shi, A. LaLonde, H. Wang, L. Chen, G. J. Snyder, *Nature* **2011**, *473*, 66.

[11] B. Yu, M. Zebarjadi, H. Wang, K. Lukas, H. Wang, D. Wang, C. Opeil, M. Dresselhaus, G. Chen, Z. Ren, *Nano Lett.* **2012**, *12*, 2077.

[12] T. Berry, C. Fu, G. Auffermann, G. H. Fecher, W. Schnelle, F. Serrano-Sanchez, Y. Yue, H. Liang, C. Felser, *Chem. Mater.* **2017**, *29*, 7042.

[13] J. P. Heremans, V. Jovovic, E. S. Toberer, A. Saramat, K. Kurosaki, A. Charoenphakdee, S. Yamanaka, G. J. Snyder, *Science* **2008**, *321*, 554.

[14] Q. Zhang, B. Liao, Y. Lan, K. Lukas, W. Liu, K. Esfarjani, C. Opeil, D. Broido, G. Chen, Z. Ren, *Proc. Natl. Acad. Sci. U. S. A.* **2013**, *110*, 13261.

[15] R. He, T. Zhu, Y. Wang, U. Wolff, J.-C. C. Jaud, A. Sotnikov, P. Potapov, D. Wolf, P. Ying, M. Wood, Z. Liu, L. Feng, N. P. Rodriguez, G. J. Snyder, J. C. Grossman, K. Nielsch, G. Schierning, *Energy Environ. Sci.* **2020**, *13*, 5165.

[16] T. Zhu, L. Hu, X. Zhao, J. He, *Adv. Sci.* **2016**, *3*, 1600004.

[17] L. Fu, M. Yin, D. Wu, W. Li, D. Feng, L. Huang, J. He, *Energy Environ. Sci.* **2017**, *10*, 2030.

[18] L. Abdellaoui, Z. Chen, Y. Yu, T. Luo, R. Hanus, T. Schwarz, R. Bueno Villoro, O. Cojocaru-Mirédin, G. J. Snyder, D. Raabe, Y. Pei, C. Scheu, S. Zhang, *Adv. Funct. Mater.* **2021**, *31*, 2101214.

[19] L. Abdellaoui, S. Zhang, S. Zaefferer, R. Bueno-Villoro, A. Baranovskiy, O. Cojocaru-Mirédin, Y. Yu, Y. Amouyal, D. Raabe, G. J. Snyder, C. Scheu, *Acta Mater.* **2019**, *178*, 135.

[20] A. Sood, R. Cheaito, T. Bai, H. Kwon, Y. Wang, C. Li, L. Yates, T. Bougher, S. Graham, M. Asheghi, M. Goorsky, K. E. Goodson, *Nano Lett.* **2018**, *18*, 3466.

[21] H. Dong, B. Wen, R. Melnik, *Sci. Rep.* **2014**, *4*, 7037.

[22] P. G. Klemens, *Int. J. Thermophys.* **1994**, *15*, 1345.

[23] A. Zevalkink, Y. Takagiwa, K. Kitahara, K. Kimura, G. J. Snyder, *Dalton Trans.* **2014**, *43*, 4720.

[24] S. Lin, W. Li, Y. Pei, *Mater. Today* **2021**, *48*, 198.

[25] E. S. Landry, M. I. Hussein, A. J. H. McGaughey, *Phys. Rev. B* **2008**, *77*, 184302.

[26] B. C. Sales, D. Mandrus, R. K. Williams, *Science* **1996**, *272*, 1325.

[27] G. S. Nolas, J. L. Cohn, G. A. Slack, S. B. Schujman, *Appl. Phys. Lett.* **1998**, *73*, 178.

[28] P. G. Klemens, in *Solid State Physics* (Eds.: F. Seitz, D. Turnbull), vol. *7*, Academic Press, Cambridge, MA **1958**, pp. 1–98.

[29] R. Hanus, M. T. Agne, A. J. E. Rettie, Z. Chen, G. Tan, D. Y. Chung, M. G. Kanatzidis, Y. Pei, P. W. Voorhees, G. J. Snyder, *Adv. Mater.* **2019**, *31*, 1900108.

[30] X. B. Zhao, X. H. Ji, Y. H. Zhang, T. J. Zhu, J. P. Tu, X. B. Zhang, *Appl. Phys. Lett.* **2005**, *86*, 62111.

[31] N. Nandihalli, D. H. Gregory, T. Mori, *Adv. Sci.* **2022**, *9*, 2106052.

[32] G. Rogl, A. Grytsiv, K. Yubuta, S. Puchegger, E. Bauer, C. Raju, R. C. Mallik, P. Rogl, *Acta Mater.* **2015**, *95*, 201.

[33] M. Zebarjadi, K. Esfarjani, M. S. Dresselhaus, Z. F. Ren, G. Chen, *Energy Environ. Sci.* **2012**, *5*, 5147.

[34] J. Zhou, H. Zhu, T.-H. Liu, Q. Song, R. He, J. Mao, Z. Liu, W. Ren, B. Liao, D. J. Singh, Z. Ren, G. Chen, *Nat. Commun.* **2018**, *9*, 1721.

[35] B. Poudel, Q. Hao, Y. Ma, Y. Lan, A. Minnich, B. Yu, X. Yan, D. Wang, A. Muto, D. Vashaee, X. Chen, J. Liu, M. S. Dresselhaus, G. Chen, Z. Ren, *Science* **2008**, *320*, 634.

[36] S. Sumithra, N. J. Takas, D. K. Misra, W. M. Nolting, P. F. P. Poudeu, K. L. Stokes, *Adv. Energy Mater.* **2011**, *1*, 1141.

[37] J. Li, J. Sui, Y. Pei, C. Barreteau, D. Berardan, N. Dragoe, W. Cai, J. He, L.-D. Zhao, *Energy Environ. Sci.* **2012**, *5*, 8543.

[38] G. Joshi, H. Lee, Y. Lan, X. Wang, G. Zhu, D. Wang, R. W. Gould, D. C. Cuff, M. Y. Tang, M. S. Dresselhaus, G. Chen, Z. Ren, *Nano Lett.* **2008**, *8*, 4670.

[39] X. W. Wang, H. Lee, Y. C. Lan, G. H. Zhu, G. Joshi, D. Z. Wang, J. Yang, A. J. Muto, M. Y. Tang, J. Klatsky, S. Song, M. S. Dresselhaus, G. Chen, Z. F. Ren, *Appl. Phys. Lett.* **2008**, *93*, 193121.

[40] T. Luo, J. J. Kuo, K. J. Griffith, K. Imasato, O. Cojocaru-Mirédin, M. Wuttig, B. Gault, Y. Yu, G. J. Snyder, *Adv. Funct. Mater.* **2021**, *31*, 2100258.

[41] J. De Boor, T. Dasgupta, H. Kolb, C. Compere, K. Kelm, E. Mueller, *Acta Mater.* **2014**, *77*, 68.

[42] Q. Qiu, Y. Liu, K. Xia, T. Fang, J. Yu, X. Zhao, T. Zhu, *Adv. Energy Mater.* **2019**, *9*, 1803447.

[43] Y. Wu, F. Liu, Q. Zhang, T. Zhu, K. Xia, X. Zhao, *J. Mater. Chem. A* **2020**, *8*, 8455.

[44] S. Wang, S. Hui, K. Peng, T. P. Bailey, X. Zhou, X. Tang, C. Uher, *J. Mater. Chem. C* **2017**, *5*, 10191.

[45] J.-H. Son, M.-W. Oh, B.-S. Kim, S.-D. Park, *Rare Met.* **2018**, *37*, 351.

[46] A. Li, C. Fu, X. Zhao, T. Zhu, *Research* **2020**, *2020*, 1934848.

[47] J. J. Kuo, S. D. Kang, K. Imasato, H. Tamaki, S. Ohno, T. Kanno, G. J. Snyder, *J. Energy Environ. Sci.* **2018**, *11*, 429.

[48] J. J. Kuo, Y. Yu, S. D. Kang, O. Cojocaru-Mirédin, M. Wuttig, G. J. Snyder, *Adv. Mater. Interfaces* **2019**, *6*, 1900429.

[49] J. J. Kuo, M. Wood, T. J. Slade, M. G. Kanatzidis, G. J. Snyder, *Energy Environ. Sci.* **2020**, *13*, 1250.

[50] K. Imasato, C. Fu, Y. Pan, M. Wood, J. J. Kuo, C. Felser, G. J. Snyder, *Adv. Mater.* **2020**, *32*, 1908218.

[51] Y. Pan, M. Yao, X. Hong, Y. Zhu, F. Fan, K. Imasato, Y. He, C. Hess, J. Fink, J. Yang, B. Büchner, C. Fu, G. J. Snyder, C. Felser, *Energy Environ. Sci.* **2020**, *13*, 1717.

[52] M. Wood, J. J. Kuo, K. Imasato, G. J. Snyder, *Adv. Mater.* **2019**, *31*, 1902337.

[53] T. J. Slade, J. A. Grovogui, J. J. Kuo, S. Anand, T. P. Bailey, M. Wood, C. Uher, G. J. Snyder, V. P. Dravid, M. G. Kanatzidis, *Energy Environ. Sci.* **2020**, *13*, 1509.

[54] R. He, D. Kraemer, J. Mao, L. Zeng, Q. Jie, Y. Lan, C. Li, J. Shuai, H. S. Kim, Y. Liu, D. Broido, C.-W. W. Chu, G. Chen, Z. Ren, *Proc. Natl. Acad. Sci. U. S. A* **2016**, *113*, 13576.

[55] P. Ying, L. Wilkens, H. Reith, N. P. Rodriguez, X. Hong, Q. Lu, C. Hess, K. Nielsch, R. He, *Energy Environ. Sci.* **2022**, *15*, 2557.

[56] W. E. Taylor, N. H. Odell, H. Y. Fan, *Phys. Rev.* **1952**, *88*, 867.

[57] A. F. Mayadas, M. Shatzkes, *Phys. Rev. B* **1970**, *1*, 1382.

[58] T. I. Kamins, *J. Appl. Phys.* **1971**, *42*, 4357.

[59] J. Y. W. Seto, *J. Appl. Phys.* **1975**, *46*, 5247.

[60] G. E. Pike, C. H. Seager, *J. Appl. Phys.* **1979**, *50*, 3414.

[61] F. Greuter, G. Blatter, *Semicond. Sci. Technol.* **1990**, *5*, 111.

[62] R. He, T. Zhu, P. Ying, J. Chen, L. Giebeler, U. Kühn, J. C. Grossman, Y. Wang, K. Nielsch, *Small* **2021**, *17*, 2102045.

[63] H. Zeng, Y. Wu, J. Zhang, C. Kuang, M. Yue, S. Zhou, *Prog. Nat. Sci.: Mater. Int.* **2013**, *23*, 18.

[64] I. Bakonyi, *Eur. Phys. J. Plus* **2021**, *136*, 410.

[65] W. D. Kaplan, D. Chatain, P. Wynblatt, W. C. Carter, *J. Mater. Sci.* **2013**, *48*, 5681.

[66] P. R. Cantwell, M. Tang, S. J. Dillon, J. Luo, G. S. Rohrer, M. P. Harmer, *Acta Mater.* **2014**, *62*, 1.

[67] P. R. Cantwell, T. Frolov, T. J. Rupert, A. R. Krause, C. J. Marvel, G. S. Rohrer, J. M. Rickman, M. P. Harmer, *Annu. Rev. Mater. Res.* **2020**, *50*, 465.

[68] C. Zhang, G. Yan, Y. Wang, X. Wu, L. Hu, F. Liu, W. Ao, O. Cojocaru-Mirédin, M. Wuttig, G. J. Snyder, Y. Yu, *Adv. Energy Mater.* **2023**, *13*, 2203361.

[69] R. J. Quinn, J.-W. G. Bos, *Mater. Adv.* **2021**, *2*, 6246.

[70] C. Fu, T. Zhu, Y. Pei, H. Xie, H. Wang, G. J. Snyder, Y. Liu, Y. Liu, X. Zhao, *Adv. Energy Mater.* **2014**, *4*, 1400600.

[71] M. K. Brod, S. Anand, G. J. Snyder, *Adv. Electron. Mater.* **2022**, *8*, 2101367.

[72] M. K. Brod, S. Guo, Y. Zhang, G. J. Snyder, *MRS Bull.* **2022**, *47*, 573.

[73] C. Fu, T. Zhu, Y. Liu, H. Xie, X. Zhao, *Energy Environ. Sci.* **2015**, *8*, 216.

[74] J. Yu, Y. Xing, C. Hu, Z. Huang, Q. Qiu, C. Wang, K. Xia, Z. Wang, S. Bai, X. Zhao, L. Chen, T. Zhu, *Adv. Energy Mater.* **2020**, *10*, 2000888.

[75] Y. Xing, R. Liu, J. Liao, C. Wang, Q. Zhang, Q. Song, X. Xia, T. Zhu, S. Bai, L. Chen, *Joule* **2020**, *4*, 2475.

[76] C. Hu, K. Xia, C. Fu, X. Zhao, T. Zhu, *Energy Environ. Sci.* **2022**, *15*, 1406.

[77] J. K. Mackenzie, *Biometrika* **1958**, *45*, 229.

[78] G. J. Snyder, A. H. Snyder, M. Wood, R. Gurunathan, B. H. Snyder, C. Niu, *Adv. Mater.* **2020**, *32*, 2001537.

[79] C. Fu, H. Wu, Y. Liu, J. He, X. Zhao, T. Zhu, *Adv. Sci.* **2016**, *3*, 1600035.

[80] K. Fletcher, P. N. Butcher, *J. Phys. C: Solid State Phys.* **1972**, *5*, 212.

[81] T. Luo, F. Serrano-Sánchez, H. Bishara, S. Zhang, B. Villoro, J. J. Kuo, C. Felser, C. Scheu, G. J. Snyder, J. P. Best, G. Dehm, Y. Yu, D. Raabe, C. Fu, B. Gault, *Acta Mater.* **2021**, *217*, 117147.

[82] R. Bueno Villoro, M. Wood, T. Luo, H. Bishara, L. Abdellaoui, D. Zavanelli, B. Gault, G. J. Snyder, C. Scheu, S. Zhang, *Acta Mater.* **2023**.

[83] K. Yamaguchi, H. Yamamoto, Y. Yamaguchi, H. Watanabe, *J. Phys. Soc. Jpn.* **1972**, *33*, 1292.

[84] A. Kjekshus, F. Grønvold, J. Thorbjørnsen, T. Briggs, G. A. D. Haslewood, H. Flood, *Acta Chem. Scand.* **1962**, *16*, 1493.

[85] G. Melnyk, W. Tremel, *J. Alloys Compd.* **2003**, *349*, 164.

[86] M. K. Miller, M. G. Hetherington, *Surf. Sci.* **1991**, *246*, 442.

[87] B. M. Jenkins, F. Danoix, M. Gouné, P. A. J. Bagot, Z. Peng, M. P. Moody, B. Gault, *Microsc. Microanal.* **2020**, *26*, 247.

[88] A. G. Hufnagel, H. Hajiyani, S. Zhang, T. Li, O. Kasian, B. Gault, B. Breitbach, T. Bein, D. Fattakhova-Rohlfing, C. Scheu, R. Pentcheva, *Adv. Funct. Mater.* **2018**, *28*, 1804472.

[89] B. W. Krakauer, D. N. Seidman, *Phys. Rev. B* **1993**, *48*, 6724.

[90] Z. Wang, C. Fu, K. Xia, F. Liu, X. Zhao, T. Zhu, *ACS Appl. Mater. Interfaces* **2021**, *13*, 7317.

[91] P.-a. Zong, R. Hanus, M. Dylla, Y. Tang, J. Liao, Q. Zhang, G. J. Snyder, L. Chen, *Energy Environ. Sci.* **2017**, *10*, 183.

[92] S. He, S. Lehmann, A. Bahrami, K. Nielsch, *Adv. Energy Mater.* **2021**, *11*, 2101877.

[93] S. Li, Y. Liu, F. Liu, D. He, J. He, J. Luo, Y. Xiao, F. Pan, *Nano Energy* **2018**, *49*, 257.

[94] H.-S. Kim, Z. M. Gibbs, Y. Tang, H. Wang, G. J. Snyder, *APL Mater.* **2015**, *3*, 41506.

[95] K. Momma, F. Izumi, *J. Appl. Crystallogr.* **2008**, *41*, 653.

[96] M. Schaffer, B. Schaffer, Q. Ramasse, *Ultramicroscopy* **2012**, *114*, 62.

[97] S. Zhang, C. Scheu, *Microscopy* **2018**, *67*, i133.

[98] K. Thompson, D. Lawrence, D. J. Larson, J. D. Olson, T. F. Kelly, B. Gorman, *Ultramicroscopy* **2007**, *107*, 131.